Catalysis Science & Technology

PAPER

View Article Online
View Journal | View Issue

Cite this: *Catal. Sci. Technol.*, 2019, **9**, 6027

Tuning mixed-phase Nb-doped titania films for high-performance photocatalysts with enhanced whole-spectrum light absorption†

Yuxin Min, Xiaoyang Yang, Dawei Wang, Kai Yang, Shisheng Zheng, Shunning Li, Haibiao Chen, Jun Liang* and Feng Pan*

Received 18th April 2019,
Accepted 17th September 2019

DOI: 10.1039/c9cy00745h

rsc.li/catalysis

Recently, the use of TiO_2 under visible (vis) light to degrade pollutants has attracted increasing attention. In our previous study, conductive anatase Nb-doped titania (NTO) thin films were demonstrated as a novel strategy to achieve good photocatalytic performance under visible light. However, the photocatalytic properties of conductive rutile NTO films are not yet known. In this study, a simple, controllable and effective method with a high deposition rate was developed to form NTO thin films with tunerable phases. By introducing a seed layer combined with suitable sputtering conditions, *e.g.* sputtering power, small crystalline clusters with rutile phase could be well controlled in the as-grown films and become a key factor to form NTO thin films with different phases. Interestingly, the NTO thin film with mixed anatase and rutile phases shows excellent photocatalytic performance due to its better absorption, more effective separation of photo-generated holes and electrons and high charge transfer. This result could bring new insight and promising application of NTO thin films in both conductive films and photocatalytic applications, particularly self-cleaning windows.

1 Introduction

Titanium dioxide (TiO_2) plays an important role in various photocatalysts not only due to its outstanding photocatalytic performance but also to its high chemical stability, low toxicity and abundance.[1–7] However, due to the wide band gap of TiO_2 (its anatase phase has a bandgap of 3.2 eV),[8] it is an ultraviolet-sensitive catalyst, which means it can only utilize ~5% of the available energy of the solar spectrum.[9] Therefore, many methods, such as ion doping,[10–19] cocatalyst modification,[20–23] heterojunction coupling[24–26] and localized surface plasmon resonance (LSPR) by noble metals,[27,28] have been introduced to enhance the response of TiO_2 in the visible range. Although all these approaches are effective, they suffer from the limited enhancement of visible light absorption or high cost. Accordingly, to obtain photocatalysts with application prospects, it is still necessary to increase the sensitivity of TiO_2 to the visible range of sunlight.

With different electrical properties and absorption characteristics from pure TiO_2, Nb-doped titania (NTO) shows potential as a photocatalytic material.[29–36] Substituting the Ti^{4+} sites by Nb^{5+} creates a Nb^{5+} defect energy level located below the bottom of the conduction band and provides electrons to the unoccupied Ti 3d orbital without introducing impurity states in the bandgap. This effect introduces more electrons into the conduction band, which assists the initial reaction of the organic decomposition process.[30,34] In addition, Nb^{5+} doping narrows the bandgap of TiO_2, which endows NTO with more intrinsic light absorption than pure TiO_2. Additionally, the doping induces shallow donor defect levels below the conduction band edge of TiO_2 and enables UV-vis-IR free carrier absorption of NTO. Due to these properties, NTO becomes sensitive to visible light.[31,32,34,35,37]

In our previous work, we reported a novel strategy to achieve anatase NTO films with a high degree of preferential orientation of the (004) planes by DC magnetron sputtering (MSP).[37,38] These (004) orientated anatase NTO films show preeminent conductive properties with decreased visible transmittance and can also be used as effective photocatalysts.[37] In addition to the crystal orientation,[37] several literature reports point out that the phase of TiO_2 also influences the photocatalytic performance.[39] Some reports claim that anatase TiO_2 shows higher photocatalytic activity,[39] while more reports demonstrated that mixed phases of anatase and rutile (such as the commercial TiO_2 powder P25, which contains 75% anatase phase and 25% rutile phase) exhibit better photocatalytic performance.[40–43]

School of Advanced Materials, Peking University Shenzhen Graduate School, 2199 Lishui Road, Shenzhen 518055, P.R. China. E-mail: liangjun@pkusz.edu.cn, panfeng@pkusz.edu.cn; Tel: +86 755 26033320

† Electronic supplementary information (ESI) available: Jade refinement, electrical property data, additional XRD patterns, transmittance spectra, additional photocatalytic degradation figures and SEM&FIB images of samples for TEM observation. See DOI: 10.1039/c9cy00745h

Thus, it is interesting to understand the relationship between the phases of conductive NTO films and their photocatalytic performance.

High power sputtering was used to produce the precursor film leading to rutile phase, and ultra-low power sputtering was used to produce the precursor film leading to anatase phase.[44] The ultra-low power process tends to be unstable and causes frequent quenching of glow plasma during the sputtering. Furthermore, low-power sputtering decreases the film growth rate and is not applicable for large area deposition. It is necessary to understand the mechanism of phase forming and develop a method to tune the phase ratio in a controllable way.

As reported, seed layers can be a useful method for film growth.[47–49] Chen *et al.* found that pre-deposition of a TiO_2 seed layer with a thickness of one unit cell could assist the epitaxial growth of heavily N-doped TiO_2 films.[47] Yamada *et al.* successfully fabricated conductive Nb-doped TiO_2 (NTO) films directly on glass instead of on a composite oxide substrate using seed layers.[48] All these reports indicate that the nano seed layer plays an important role in the growth of thin films. Therefore, we attempted to introduce nano seed layers to grow NTO films with controllable ratios of anatase and rutile phase.

In this work, small crystalline clusters with rutile phase were found to be the key factor to form NTO thin films with different phases. By adjusting the sputtering power, small crystalline clusters could be controlled to form rutile phase. After annealing, these films showed good crystallization with different phases. Additionally, in order to eliminate the influence of the sputtering power on the photocatalytic performance, a seed layer was introduced to achieve pure anatase NTO thin films under a high sputtering power. We obtained highly conductive NTO films by depositing a precursor film using DC magnetron sputtering and then post-annealing in a reduction environment. Furthermore, the surface morphologies, electrical properties, optical properties, energy band structures and photocatalytic performance of the films were studied. Interestingly, the NTO thin film with mixed anatase and rutile phases exhibited excellent photocatalytic performance due to its better absorption, more effective separation of photo-generated holes and electrons and high charge transfer. By comparison with pure TiO_2 films, the extended free-carrier absorption (FCA) effect caused by Nb-doping was determined, which explains the better photocatalytic performance of the NTO films. This result could bring new insight and promising application of NTO thin films in both conductive films and photocatalytic applications, especially self-cleaning windows.

2 Experimental section

2.1 General film preparation

NTO films with random orientation were deposited by DC magnetron sputtering with the substrate placed vertically to the sputtering direction. The distance between the center of the target and the substrate was 8 cm. Films were deposited in pure argon (grade 5.0) at a flow rate of 20 sccm (cubic centimeter per minute at STP) and a system pressure of 0.3 Pa. The substrate temperature during deposition was maintained at 40 °C to 60 °C. Before each deposition, the target surface was sputter-cleaned by pure Ar for 10 min and then pre-sputtered for 5 min under the deposition conditions. A DC sputtering power system (SKY Technology Development DC power system) was used. The sputtering duration was adjusted according to the power used in each deposition to prepare films with thicknesses in the range of 300 to 400 nm.

NTO thin films without an anatase phase seed layer (NTO-G) were sputtered onto 3 × 3 cm^2 soda-lime glass substrates (GULUO GLASS) using an oxide target (Φ 6 cm) with 5 at% of Nb dopant ($Ti_{0.95}Nb_{0.05}O_2$, 99.9%). NTO thin films with anatase phase seed layers (NTO-SL) were sputtered onto about 2 × 2 cm^2 seed layer substrates cut from a 10 × 10 cm^2 substrate with a seed layer. The 10 × 10 cm^2 soda-lime glass (GULUO GLASS) substrate for the seed layers was pre-deposited by the same DC magnetron sputter method using an oxide target (10 × 20 cm^2) with 5 at% Nb dopant ($Ti_{0.95}Nb_{0.05}O_2$, 99.9%) for a very short period (about 2 min) with ultra-low power. Then, the film was annealed in air at 450 °C for 60 min to obtain the substrate with a seed layer. The 3 × 3 cm^2 soda-lime glass substrate and 2 × 2 cm^2 substrate with a seed layer were secured onto a stainless steel substrate holder with polyamide tape. The as-deposited films were annealed in Ar/H_2 (95 : 5, v/v) atmosphere at a flow rate of 30 sccm in a tube furnace at 400 °C for 60 min with a ramp rate of 10 °C min^{-1}. The annealed samples were naturally cooled to room temperature.

Non-doped TiO_2 thin films were prepared in the same way using a Φ 6 cm oxide target.

2.2 Film analysis

The crystal structures of the NTO films were analysed using a Bruker D8 Advance powder X-ray diffractometer (XRD) equipped with CuKα radiation with a two-dimensional detector.

The electrical properties of the films were measured at room temperature on an Ecopia HMS-3000 Hall effect measurement system set up in the Van der Pauw configuration in a clean room. Measurements were carried out on 1 × 1 cm^2 squares, and a standard ITO sample was tested prior to any NTO thin film measurements.

Optical properties were analysed over the wavelength range of 300 to 800 nm using a Shimadzu UV-2450 spectrometer with an integrating sphere. The reference sample was freshly prepared from anhydrous $BaSO_4$ powder.

The thicknesses of the films were measured using a Bruker DektakXT profilometer.

The morphologies of the thin films were observed using a Zeiss SUPRA-55 scanning electron microscope (SEM).

The surface morphologies, roughnesses and specific areas of the thin films were measured and analysed with a Bruker MultiMode 8 atomic force microscope (AFM) using tapping mode with SCM-PIT probes.

Microstructures were observed using a JEOL JEM2010-FEF high resolution transmission electron microscope (HRTEM). The cross-sections of the NTO films for TEM observation were prepared using an FEI Scios Dual Beam FIB SEM. The interplanar spacings were calculated from the corresponding diffraction spots in the fast Fourier transform (FFT) images. The content of Nb was investigated *via* an Oxford X-Max 100TLE energy dispersive spectrometer (EDS).

Photographs were taken using the camera in a Mi 6 mobile phone.

2.3 Catalytic activity tests

Photocatalytic degradation of rhodamine B (Rh B) under simulated solar light irradiation. The annealed NTO films were cleaned by ultrasonic treatment in aqueous solutions of detergent, deionized water, ethanol, and isopropyl alcohol, sequentially, for 15 min each step, and then dried under N_2 flow. The ethanol solution of Rh B dye was prepared to a concentration of 2000 ppm. The Rh B solution was coated onto the NTO film surface and dried on a hot-plate at 80 °C. The initial absorbances of the NTO films covered with Rh B coatings were measured using a UV-vis spectrophotometer (Shimadzu UV-2450), then irradiated under AM 1.5 illumination *via* an ABET sun 3000 solar simulator. The power of the light was calibrated to one sun light intensity using an NREL-calibrated Si cell (Oriel 91150). The maximum absorbance of Rh B was recorded periodically.[37,45] The amount of Rh B was estimated by the Lambert–Beer law, where the absorbance is proportional to the concentration of a dilute solution. From that, the degradation of Rh B could be described as follows:[36,46]

$$\frac{C_0}{C} = \frac{A_0}{A} \tag{1}$$

$$\ln\frac{C_0}{C} = kt \tag{2}$$

where C_0 is the initial concentration of the Rh B solution, C is the concentration at a specific irradiation time, A_0 is the initial absorbance of the Rh B solution, A is the absorbance at a specific irradiation time, k is the reaction rate constant, and t is the reaction time. We assumed that this law applies to Rh B molecules on the surface of thin films.

2.4 TiO_2 band calculation

The band structures of rutile and anatase TiO_2 were calculated using density-functional theory (DFT). All the computations were performed by means of density functional theory using the Vienna *ab initio* simulation package (VASP) with the HSE06 (ref. 51 and 52) screened hybrid exchange functional and the projector augmented wave (PAW) method.[53] A 450 eV cut-off energy for the plan wave basis set was adopted. The convergence criteria of energy and force were 10^{-5} eV and 0.02 eV $Å^{-1}$, respectively. The band alignment was calculated by referencing the valence and conduction bands of a specific surface to the vacuum level.[54,55] The ionization potential (IP) and electron affinity (EA) of rutile and anatase TiO_2 were investigated to estimate interfacial band offsets. The band structures of different TiO_2 polymorphs along the high symmetry direction in the Brillouin zone were computed. The band alignments of these two polymorphs were investigated by calculating the IP and EA. Supercells consisting of 2 × 2 × 2 unit cells were constructed for the investigation of Nb-doped TiO_2, in which one Ti atom was substituted by Nb. *k*-Point meshes of 4 × 4 × 6 and 5 × 5 × 4 were used for the calculations of the electronic structures of the rutile and anatase phases, respectively.

3 Results and discussion

3.1 Conditions for controllable phase formation

The as-grown NTO thin film was firstly prepared on glass using a DC magnetron sputter with sputtering powers of 40 W, 60 W, 80 W, 100 W, 120 W and 140 W, corresponding to power densities of 1.41, 2.12, 2.83, 3.54, 4.24 and 4.95 W cm^{-2}, respectively, for an oxide target 6 cm in diameter. After annealing at 400 °C for 1 h in Ar/H_2 (95 : 5, v/v) atmosphere, the NTO films showed good crystallization.

According to the XRD results in Fig. 1a, the films deposited onto bare soda-lime glass (abbreviated "G") under the sputtering powers of 40 W and 60 W were pure anatase. The films deposited under the sputtering powers of 80 W and 100 W were found to be mixed phases of anatase and rutile. When the sputtering power exceeded 120 W, the films were found to be mainly rutile. The content of rutile phase was calculated using the empirical formula:[61–63]

$$\%\text{Rutile} = 0.679\left(\frac{I_R}{I_R + I_A}\right) + 0.312\left(\frac{I_R}{I_R + I_A}\right)^2 \tag{3}$$

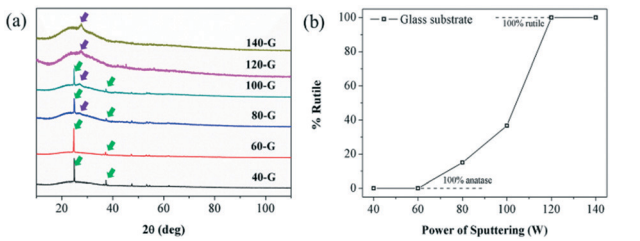

Fig. 1 (a) X-ray diffraction patterns of annealed NTO thin films deposited onto soda-lime glass substrates (marked with "G") with sputtering powers of 40 W, 60 W, 80 W, 100 W, 120 W and 140 W. The green arrows mark the (101) and (004) characteristic peaks of anatase phase, while the purple arrows mark the (110) characteristic peak of rutile phase. (b) Phase ratio of annealed NTO thin films deposited onto soda-lime glass substrates.

where I_A is the intensity of the main anatase characteristic (101) peak at 2θ = 24.7° and I_R is the intensity of the main rutile characteristic (110) peak at 2θ = 26.9°. Peak area instead of peak height was used to represent the intensities of the peaks. The calculations showed that there was 15.0% rutile phase in film 80-G and 36.7% rutile phase in film 100-G. The rutile content is closely related to the sputtering power, as is clearly shown in Fig. 1b. Therefore, adjusting the sputtering power is a feasible way to control the phase compositions of NTO films.

We speculate that the clusters formed in the sputtering process can determine the final phase of the bulk film after annealing. NTO films with anatase phase were preferentially formed because of the spontaneous annealing crystallization of TiO_2. The NTO thin films with rutile phase and mixed phases can be attributed to the controllable formation of small crystalline clusters with rutile phase in the as-grown films. To verify this hypothesis, typical films with different deposition conditions were studied by TEM observation, as shown in Fig. 2. The TEM images and fast Fourier transform (FFT) algorithm images were systematically studied, as shown in Fig. 2. No obvious crystal region could be found in the as-grown film 40-G (Fig. 2a). After annealing, obvious anatase crystallization was found both in the XRD results (Fig. 1a) and in the TEM images (Fig. 2g) and fast Fourier transform (FFT) algorithm images (Fig. 2h and i). Compared with the characteristic peaks of the possible crystal phases, the (101) and (004) crystal planes of anatase TiO_2 matched interplanar spacings of 0.3514 and 0.2366 nm, respectively. These crystalline interplanar spacing data come from the standard PDF cards of XRD, calculated using the Bragg equation.

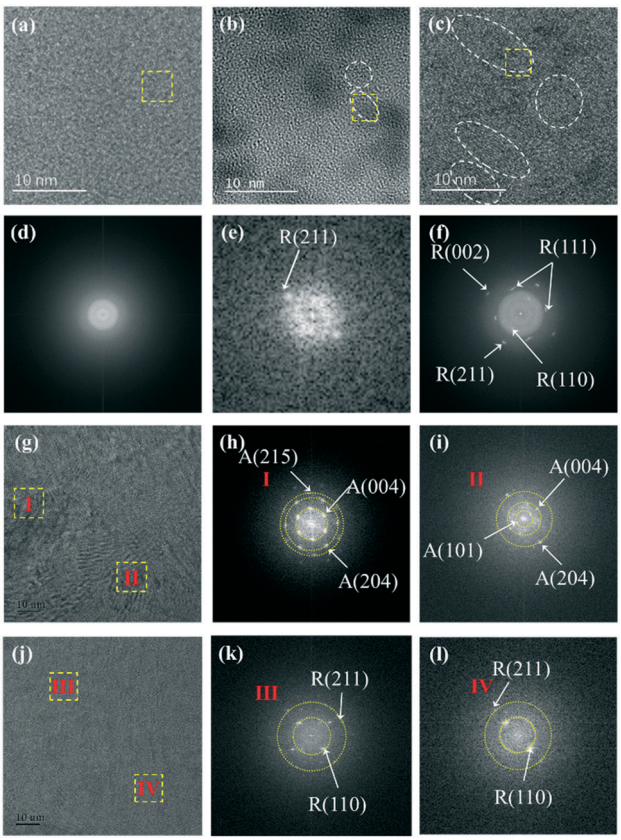

Fig. 2 TEM images of (a) as-grown NTO 40-G, (b) as-grown NTO 80-G, (c) as-grown NTO 120-G, (g) annealed NTO 40-G and (j) annealed NTO 120-G. (d), (e) and (f) FFT algorithm images of (a), (b) and (c) from the yellow square regions, respectively. The crystal region is marked by a white circle. (h) and (i) FFT algorithm images of (g) from the yellow square region. (k) and (l) FFT algorithm images of (j) from the yellow square region. "A" indicates anatase phase, while "R" indicates rutile phase.

These results demonstrated that NTO films with anatase phase were preferentially formed because of the spontaneous annealing crystallization of TiO_2. The as-grown films 80-G (Fig. 2b) and 120-G (Fig. 2c) showed many nanocrystal clusters (sizes about 5 to 10 nm) with rutile phase. These nanocrystal clusters were marked by white circle regions and were determined by the TEM images (Fig. 2b and c) and FFT patterns (Fig. 2e and f). The dots in the FFT images were identified as rutile phase, as shown in Fig. 2e and f, because the interplanar spacing of the (110) crystal planes was 0.334 nm, which can only be fitted to the rutile (110) crystal plane, where rutile TiO_2 has an interplanar spacing of 0.3203 nm. The crystallized areas (circled by white dotted lines) in Fig. 2b and c show average interplanar spacings of about 0.338 nm, which correspond to the former result. The increase of the interplanar spacing from the normal value can be explained by the fact that niobium doping enlarges the unit cells because the ionic radius of Nb^{5+} (*ca.* 0.70 Å) is slightly larger than that of Ti^{4+} (*ca.* 0.68 Å). This effect also can be seen in the XRD results, where the characteristic peaks shift to low angles compared to undoped titanium dioxide. After annealing, obvious rutile crystallization was found both from the XRD results (Fig. 1a) and from the TEM image (Fig. 2j) and fast Fourier transform (FFT) algorithm images (Fig. 2k and l). These results demonstrated that the NTO films with rutile phase originated from the small rutile crystalline clusters. Thermodynamically, the spontaneous anatase annealing crystallization of TiO_2 competed with the growth of the small rutile crystalline clusters. Therefore, anatase and rutile mixed phases were formed in film 80-G.

As mentioned above, the phases of the small crystal clusters in the as-grown films deeply influenced the final crystalline phases of the annealed films. The formation of these clusters could be adjusted by simple, controllable and effective methods, such as changing the sputtering power. However, changing the sputtering power can seriously influence the surface morphologies of films and result in enormous differences in their photocatalytic performance. In order to eliminate the influence of the sputtering power, we introduced an anatase nano seed layer to achieve anatase thin films under a high sputtering power.

3.2 The introduction of the anatase nano seed layer

According to the above analysis, the small crystal clusters play important roles in the crystallization during annealing. Herein, we introduced an anatase nano seed layer as a new deposition substrate.

The thickness of the seed layer was so small (only about 10 to 20 nm according to the HRTEM pattern of the cross section, Fig. 3a) that no characteristic peaks could be identified by XRD. Only the amorphous phase of the glass substrate was found, as shown in Fig. S2 in the ESI.† Therefore, the phase of the nano seed layer was determined to be anatase by local FFT (Fig. 3b) of the TEM image (Fig. 3a).

Interestingly, the introduction of the seed layer could stably form anatase phase in the thin films when the sputtering power was below 120 W, as shown in Fig. 4a. Obviously, NTO films with both anatase phase and rutile phase were successfully achieved under a high sputtering power. To explain this fantastic result, we performed the preceding FIB sampling and TEM studies on the as-grown film (marked as film 120-SL) under the sputtering power of 120 W. As shown in Fig. 3c and d, when an anatase seed layer exists, there is no formation of rutile clusters in the as-grown film 120-SL. Contrastingly, thin films with rutile phase were prepared on the glass substrate under the sputtering power of 120 W.

These results indicate that an anatase seed layer can greatly restrain the formation of rutile clusters when the sputtering power is below 120 W. It should be noted that some rutile phase could be found in the NTO thin film 120-SL, suggesting that the sputtering power should be maintained below 120 W to prevent the formation of rutile phase with an anatase seed layer. These thin films were also collected and marked as film 120-A + R. When the sputtering power increased to 140 W, rutile became the main phase despite the presence of the seed layer. It appears that the introduction of an anatase seed layer cannot prevent the formation of rutile clusters.

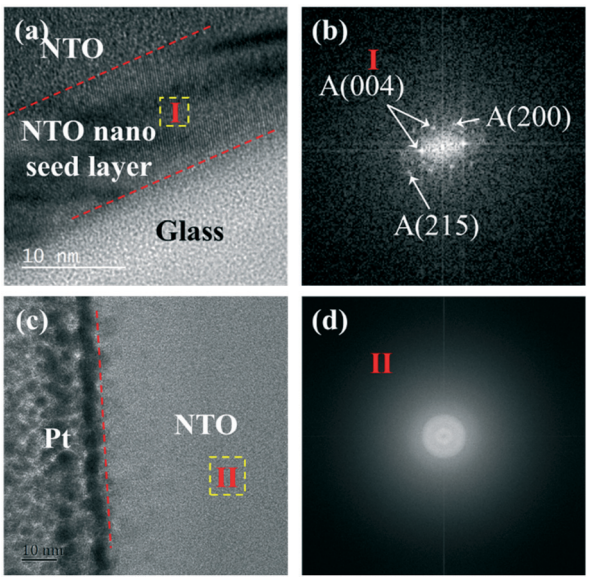

Fig. 3 TEM image of the NTO seed layer substrate (a); the FFT image of the yellow square region of (a) is shown in (b). TEM image of the NTO film 120-SL (c); the FFT image of the yellow square region of (c) is shown in (d).

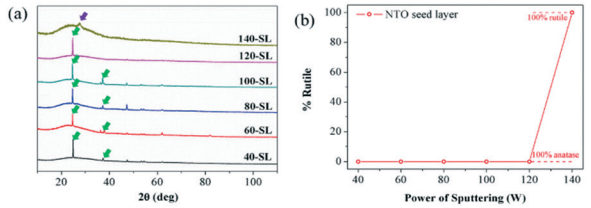

Fig. 4 X-ray diffraction patterns of annealed NTO thin films deposited onto NTO nano seed layer substrates (marked with "SL") with sputtering powers of 40 W, 60 W, 80 W, 100 W, 120 W and 140 W. The green arrows mark the (101) and (004) characteristic peaks of anatase phase, while the purple arrows mark the (110) characteristic peak of rutile phase. (b) Phase ratios of annealed NTO thin films deposited onto NTO nano seed layer substrates.

To study the relationship between the phase composition and the photocatalytic performance, a special NTO film, 120-A + R, was prepared; it showed prominent characteristic XRD peaks (see ESI,† Fig. S3-1) for both anatase and rutile phase. This "120-A + R" film was deposited onto a seed layer substrate at a power of 120 W, and the thickness was about 700 nm (nearly twice those of the other samples). There was 68.4% rutile phase in the NTO film 120-A + R as estimated using the same empirical formula (eqn (3)), as shown in Fig. S1-1 in the ESI† and Fig. 5b.

As mentioned above, the introduction of an anatase nano seed layer can function as an anatase template, induce anatase growth, and assist the formation of pure anatase films under a high sputtering power, which verified the hypothesis we proposed earlier. This result enables us to compare the photocatalytic performance of anatase and rutile films. Moreover, it also allows us to grow pure anatase films in a wider range of sputtering conditions, which has important significance in commercial processes for novel NTO conductive thin films.

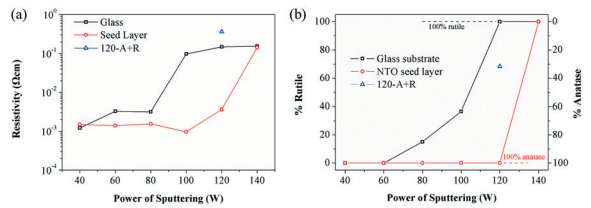

Fig. 5 (a) The relationship between the electric resistivity and the sputtering power of the NTO films. (b) The relationship between the crystal phase and the sputtering power of the NTO films. The black lines represent the films deposited on bare glass substrate, while the red lines represent the films deposited on the substrate with a NTO nano seed layer. The blue triangle points are the special film 120-A + R.

3.3 Electrical properties of NTO films with different crystal phases

The electrical properties of NTO thin films are important for their photo-generated charge transfer and can influence their photocatalytic performance. The electrical properties of the films were characterized by the standard four-probe Hall-effect measurements. The measurements indicate that the NTO films show n-type conductivity; the dominant charge carrier in the Hall effect is electrons because of the oxygen vacancies generated by Nb^{5+} doping. The sheet resistances of the as-grown films are too high (about 0.5 to 7 MΩ, as measured by a two-point probe method using an Agilent Millimeter instrument) to be tested with standard four-probe Hall-effect measurements.

After being annealed in a reducing atmosphere, the NTO films crystallized and scattering of the charge carriers at the grain boundaries decreased significantly, resulting in high conductivity. As listed in Table S1 in the ESI,† the electrical properties of the annealed films are mainly determined by their phase constituents. The pure anatase films show electrical resistivities of 10^{-3} to 10^{-4} Ω cm, which are comparable to the ITO films. The mixed phase films with mainly anatase and little rutile phase show a higher resistivity of 10^{-2} Ω cm. As the rutile phase increases, the resistivity is as high as 10^{-1} Ω cm. These results indicate that the resistivity of rutile phase is at least two orders of magnitude higher than that of anatase phase, as shown in Fig. 5a. The difference in the resistivities of these two phases can be mainly ascribed to the much lower carrier mobility in rutile phase.[59,60]

When an anatase nano seed layer is introduced, the conductivity of the thin films is significantly enhanced. As shown in Fig. 5a, the resistivity of the film with a seed layer remained at 10^{-3} Ω cm even when the sputtering power was as high as 120 W; however, the resistivity of the film deposited onto bare glass soon increased to 10^{-1} Ω cm, even when the power was only 100 W. Therefore, the introduction of an anatase nano seed layer has important significance in commercial processes for novel NTO conductive thin films.

Specifically, the NTO thin film 120-A + R is marked by blue triangle points in Fig. 5a and b. With 68.4% rutile phase and 31.6% anatase phase in this film, the resistivity is as high as 3.6×10^{-1} Ω cm. This can be ascribed to the excessive thickness of film 120-A + R (about twice those of the other films). The sheet resistance of this film is at the same level as those of the other rutile films; however, when calculating the sheet resistivity, the thickness value must be multiplied.

3.4 Physical properties and surface morphologies of NTO thin films with different crystal phases

The light absorption ability of TiO_2 is an important factor influencing its photocatalytic performance. The UV-vis reflectance spectra of NTO films 120-SL, 120-G and 120-A + R are shown in Fig. 6a. The Kubelka–Munk absorption spectra of NTO films 120-SL, 120-G and 120-A + R were converted

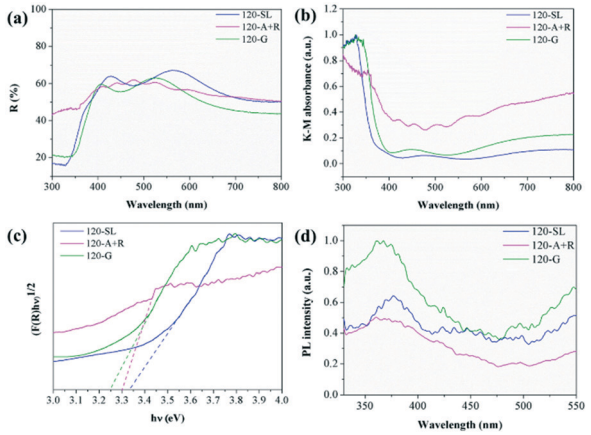

Fig. 6 (a) Diffuse reflectance spectra of 120-SL, 120-G and 120-A + R. (b) The Kubelka–Munk absorption spectra of the thin films converted from DRS by K–M manipulation. (c) Intrinsic optical absorption edges (eV) of the thin films. (d) Photoluminescence (PL) spectra of the thin films with 300 nm laser excitation.

from the reflectance spectra using the Kubelka–Munk method and are shown in Fig. 6b. The results indicate that NTO thin films 120-SL, 120-G and 120-A + R can absorb visible light. It should be noted that within the visible light range (370 to 800 nm), the NTO thin film 120-A + R has higher absorption than the other two samples. The visible light absorption can be partly ascribed to the existence of Ti^{3+} and O vacancies; however, the X-ray photoelectron spectroscopy (XPS) spectra (Fig. S5 in the ESI†) indicate that the relative amount of Ti^{3+} was not the dominant factor to explain this difference.

The intrinsic optical bandgaps of these NTO films were calculated by constructing Tauc plots using the $(\alpha h\nu)^n$ relation. The coefficient should be 1/2 because NTO is an indirect bandgap semiconductor, like TiO_2. The value of the Tauc gap (E_g) can be evaluated from the intercept on the energy axis by extrapolating the high-energy points to the position of zero absorption. As shown in Fig. 6c, the band gaps range slightly from 3.25 eV to 3.34 eV. The NTO film 120-G (green line), which contains mostly rutile phase, has the narrowest bandgap (3.25 eV) among the samples, while the film 120-A + R (pink line) with mixed phases has an intermediate bandgap of 3.30 eV. NTO film 120-SL with pure anatase phase shows the widest bandgap of 3.34 eV. This result indicates that rutile NTO has a narrower bandgap than anatase NTO, and the presence of rutile phase can narrow the bandgap of the NTO film. This result is in good agreement with our calculations for rutile phase and anatase phase TiO_2-based materials.

Fig. 7a and b is the electronic band structure of rutile and anatase phase calculated by using the density-functional theory (DFT), and the result was very close to the work of M. Landmann *et al.*[50] The band gap values for rutile and anatase TiO_2 are 3.31 eV and 3.73 eV, respectively, matching well with the trends in previous hybrid-functional work.[50,56,57] The calculated bandgaps are wider than our measurement data;

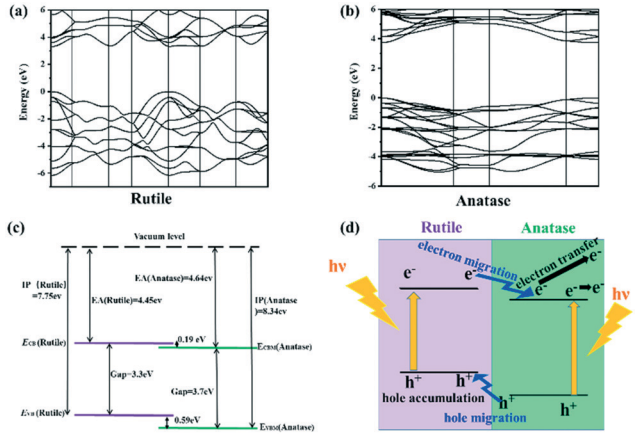

Fig. 7 (a) Band structures of rutile TiO_2. (b) Band structure of anatase TiO_2. (c) Band alignment of rutile and anatase phase. (d) Schematic diagram of charge migration and electron transfer.

this is because Nb^{5+}-doping narrows the bandgap significantly by forming some shallow donor levels below the conduction band edge.[34,35]

Fig. 6d shows the normalized photoluminescence (PL) emission spectra of films 120-SL, 120-A + R and 120-G under 300 nm laser excitation. The general trend of PL emission intensity is 120-G (rutile) > 120-SL (anatase) > 120-A + R (mixed phases). This indicates that the mixed anatase and rutile phases can decrease the PL intensity and lower the radiative recombination of photo-excited electron–hole pairs. This improvement of charge separation in the mixed phase film can be explained by the electronic band structures of TiO_2-based materials. As shown in Fig. 7c, the conduction band of anatase phase is more negative than that of rutile phase. The ionization potentials (IP) of rutile and anatase are 8.34 eV and 7.75 eV, respectively, indicating that the VBM of rutile lies 0.59 eV above that of anatase. The CBM of rutile also lies above the anatase by a value of 0.19 eV, which is in agreement with previous studies using different computational methods.[56,58] The results indicate that in mixed phases, the difference in the conduction band between rutile and anatase phases allows the photo-generated electrons to transfer from the conduction band of rutile to the conduction band of anatase.[42,43] However, the existence of an energy barrier inhibits anti-migration; thus, the migrating electrons can quickly move to the surface of anatase due to their high conductivity. In the same way, holes will accumulate in rutile phase, as shown in the schematic in Fig. 7d. This effect facilitates the separation of electrons and holes and prolongs the lifetimes of both carriers, potentially leading to enhancement of the photocatalytic performance. The difference in the charge separation behaviours between film 120-G and film 120-SL can be attributed to their difference in conductivity. The high conductivity of anatase phase helps the photo-generated electrons to separate instead of recombine, as they do in rutile phase.

AFM images of typical 500 nm × 500 nm areas of the NTO thin films with different crystalline phases are shown in

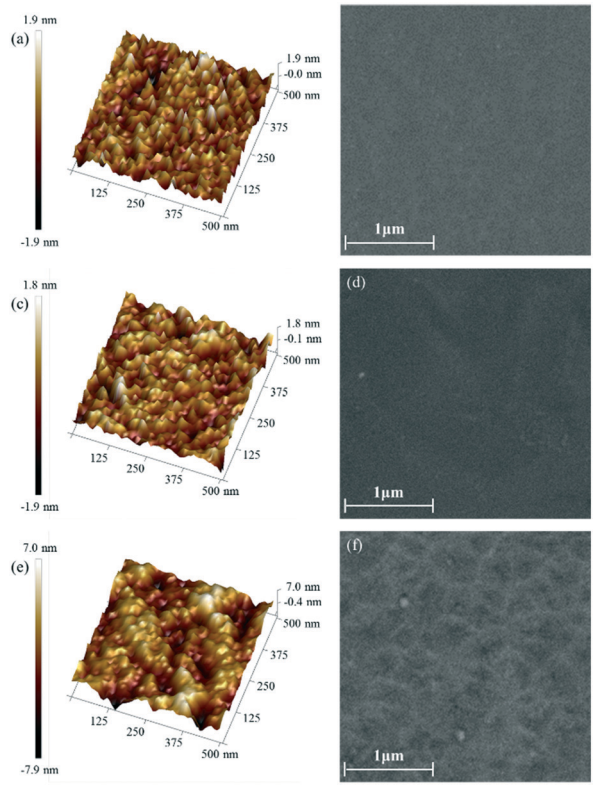

Fig. 8 AFM 3D images and top-down SEM images of the annealed thin films 120-SL (a and b), 120-G (c and d) and 120-A + R (e and f).

Fig. 8. The root-mean-square roughnesses (R_q) are 0.53, 0.52 and 2.09 nm for NTO films 120-SL, 120-G and 120-A + R, respectively. The AFM results indicate that all these NTO thin films are compact and smooth. Correspondingly, the calculated surface areas are 0.2508, 0.2505 and 0.2538 μm^2 for NTO films 120-SL, 120-G and 120-A + R, respectively. These results indicate that the surface areas of NTO films 120-SL, 120-G and 120-A + R have little difference.

3.5 Photocatalytic abilities of the NTO films

The photocatalytic performance of the NTO films was measured by the light degradation of rhodamine B (Rh B)

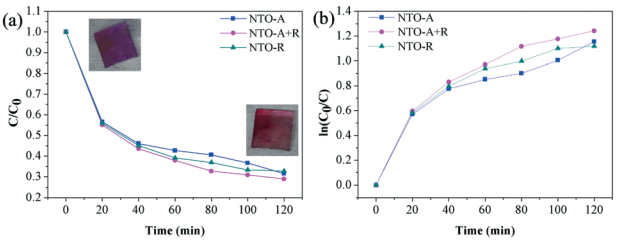

Fig. 9 (a) Comparison of the photocatalytic degradation rates of Rh B for films NTO-A, NTO-R and NTO-A + R. The comparison photos before (0 min) and after (120 min) photocatalytic degradation are shown in the insert images. (b) The reaction rates (k-value) of photocatalytic degradation for the NTO films NTO-A, NTO-R and NTO-A + R.

dye which was surface coated on the NTO films (Fig. S6 in ESI†). Rh B is a carcinogenic dye compound which is often used as a model molecule for photocatalytic degradation. The NTO films with all three different phase compositions showed considerable ability to degrade Rh B under simulated AM 1.5 solar light irradiation (100 mW cm^{-2}) at a constant temperature of 25 °C (Fig. 9a). However, there were differences in the photocatalytic performance of these three NTO films. Here, we marked sample 120-SL as "NTO-A" due to its high content of anatase phase. In the same way, sample 120-A + R was marked as "NTO-A + R", and sample 120-G was marked as "NTO-R." As shown in Fig. 9, the sample NTO-A + R (with mixed phases) showed the best photocatalytic performance.

This can be ascribed to the better absorption, more effective separation of photo-generated holes and electrons and high charge transfer. Firstly, the NTO-A + R (mixed phases) and NTO-R (rutile) films showed better absorption than the NTO-A film (anatase) because rutile phase has a narrower band gap than anatase, which means rutile phase can absorb light with lower energy. Moreover, the difference between the band levels of anatase and rutile phases aids the migration of photo-generated electrons from rutile to anatase phase. As a result, holes accumulate in the rutile phase; thus, the NTO film with mixed phases shows excellent photocatalytic performance. Finally, the NTO film with mixed phases also has good anatase phase conductive channels. These channels aid fast migration of electrons to the surfaces of the films and promote effective charge carrier separation. Therefore, the mixed phase NTO film achieved the best photocatalytic performance.

Although film NTO-A (anatase) has a wider band gap, which limits the capacity factor of sunlight, NTO-A shows comparative performance to NTO-R (rutile). This may be due to the higher conductivity of anatase films, which facilitates the separation of electrons and holes during the catalysis process. Although the film NTO-R with pure rutile phase can absorb lower energy light, the poor conductivity increases the possibility of electron–hole recombination, which decreases its photocatalytic performance.

Although the photocatalytic ability of thin films is highly dependent on their surface morphology,[40] the surface areas of these films calculated from the AFM data are almost identical and very close to the geometrical areas of the thin films because the surfaces of these films are all compact and smooth and have very little difference in roughness, as shown in Fig. 8. For film NTO-A + R, its best photocatalytic performance can be partly ascribed to its largest roughness and surface area. However, when comparing the films NTO-R and NTO-A, the very slight difference in roughness cannot explain their different photocatalytic performance. These results indicate that the photocatalytic performance of the NTO thin films in this study is not exceptionally dependent on their surface area and roughness. In other words, the crystal phases and electric properties of the NTO thin films are key factors influencing their photocatalytic abilities.

It should be noted that there are two main processes in the degradation of Rh B: the cleavage of the conjugate ring (the chromophoric group) and *N*-deethylation. The conjugate ring cleavage (called complete degradation) leads to a decrease of the highest absorption peak, while the *N*-deethylation process (called incomplete degradation) leads to a blue shift of the absorption peak. According to the absorption spectra in Fig. S6 in the ESI,† complete and incomplete degradation of Rh B could be identified. When the complete degradation is not enough, as with the film NTO-A (Fig. S6a in the ESI†), the degradation rate constant k will decrease after a certain irradiation time.

Non-doped TiO_2 films were prepared in the same way for comparison with the NTO films. Like the NTO films, these non-doped TiO_2 films were marked as TiO_2-A (anatase), TiO_2-R (rutile) and TiO_2-A + R (mixed phase of anatase and rutile), respectively. As Fig. 10 shows, for all three crystalline phases, the Nb-doped TiO_2 films show better photocatalytic performance than the non-doped films. This phenomenon can also be ascribed to the electronic properties. For the pure TiO_2 films, because no extra electrons were added by defects, the conductivities of all the TiO_2 films were much poorer than those of the Nb-doped films, which is unfavourable for the separation of photo-generated holes and electrons. Furthermore, although the band structures did not change greatly, the Fermi level was located at the bottom of the conductive band (Fig. 11b and d) after Nb-doping. This induces storage of free electrons in the shallow defect level beneath the conductive band, and these electrons can be easily excited by visible light. The increase of absorbance can be called "free carrier absorption" (FCA). The FCA effects are shown in Fig. S9 in the ESI.† From Fig. 10d, it can be seen that the mixed phase film TiO_2-A + R shows the best photocatalytic performance, consistent with the Nb-doped

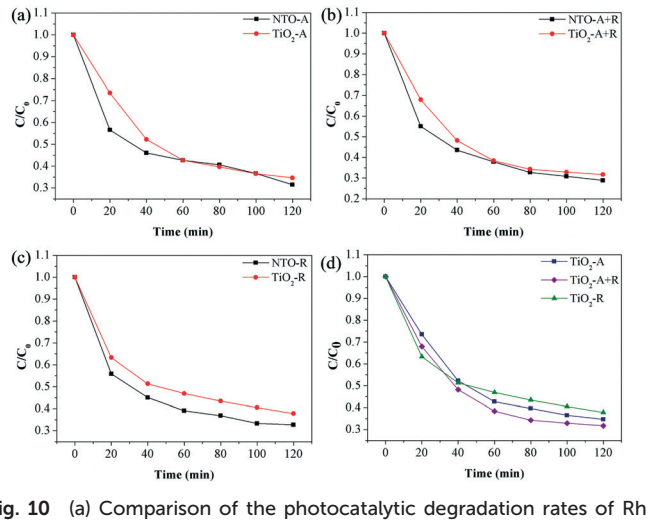

Fig. 10 (a) Comparison of the photocatalytic degradation rates of Rh B for films NTO-A and TiO_2-A. (b) Comparison of the photocatalytic degradation rates of Rh B for films NTO-A + R and TiO_2-A + R. (c) Comparison of the photocatalytic degradation rates of Rh B for films NTO-R and TiO_2-R. (d) Comparison of the photocatalytic degradation rates of Rh B for films TiO_2-A, TiO_2-R and TiO_2-A + R.

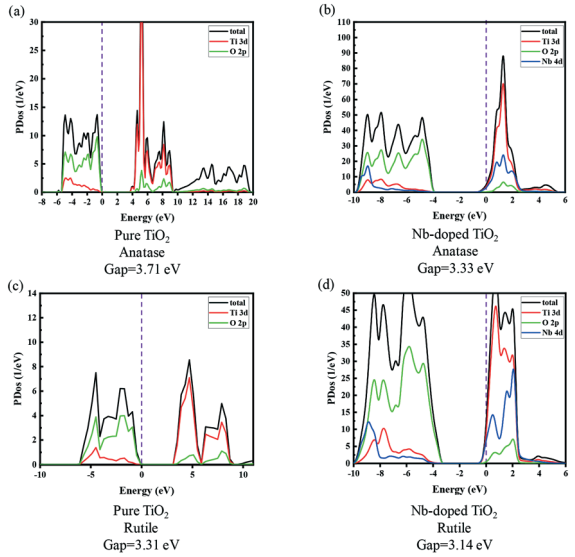

Fig. 11 (a) DOS (density of states) of pure TiO_2 with anatase phase. (b) DOS (density of states) of Nb-doped TiO_2 with anatase phase. (c) DOS (density of states) of pure TiO_2 with rutile phase. (d) DOS (density of states) of Nb-doped TiO_2 with rutile phase. The Fermi level is at zero energy and is marked by the purple dashed line. The DOS of the Nb-d states are multiplied by 10 to facilitate visualization.

TiO_2 films. Furthermore, all six films we tested could decompose most of the Rh B on the surface after 14 hours of irradiation (Fig. S10 in ESI†).

Overall, the surface morphologies, electrical properties, optical properties, energy band structures and photocatalytic performance of Nb-doped TiO_2 and pure TiO_2 films were studied. Interestingly, the thin film with mixed anatase and rutile phase shows excellent photocatalytic performance due to its better absorption, more effective separation of photo-generated holes and electrons and high charge transfer. Nb-doping extends the capacity to use visible light; thus, the NTO films show better photocatalytic performance than the pure TiO_2 films. This result may provide a new view of NTO thin films in both conductive films and photocatalytic applications, especially self-cleaning windows.

4 Conclusions

In summary, we developed a feasible method to obtain NTO thin films with anatase, rutile and mixed anatase–rutile phases. It was found that small crystalline clusters of rutile phase in the as-grown films are the key factor to form NTO thin films composed of single rutile or mixed phases. These clusters could be controlled by adjusting the sputtering conditions, *e.g.* the sputtering power. Moreover, the introduction of an anatase nano seed layer enabled us to achieve pure anatase NTO thin films under a high sputtering power. This is highly significant to the visible light photocatalytic application of these novel NTO conductive thin films. Furthermore, their surface morphologies, electrical properties, optical properties, energy band structures and photocatalytic performance were systematically studied. The mixed phase NTO film with 68.4% rutile and 31.6% anatase phases showed better photocatalytic performance than both the pure anatase and rutile phase films. The key factors of excellent photocatalytic performance were attributed to the good absorption, effective photo-generated carrier separation and high charge transfer. By comparison with pure TiO_2 films, the FCA effect was determined to be caused by Nb-doping, which explains the better photocatalytic performance of the NTO films. Finally, some new insights and promising applications of NTO thin films in both conductive films and photocatalytic applications, especially self-cleaning windows, can be expected.

Conflicts of interest

There are no conflicts to declare.

Acknowledgements

This work was financially supported by the Shenzhen key science and technology plan (Grant No. JSGG20141118144410953), the Guangdong applied technology research special project (Grant No. 2015B090927003), and the Shenzhen Science and Technology Innovation Committee (Grant No. JCYJ20150331101121646 and No. KQJSCX20180323174713505).

Notes and references

1 C. Haihan, C. E. Nanayakkara and V. H. Grassian, *Chem. Rev.*, 2012, **112**(11), 5919–5948.
2 A. Fujishima and K. Honda, *Nature*, 1972, **238**(5358), 37–38.
3 A. Fujishima, X. Zhang and D. A. Tryk, *Surf. Sci. Rep.*, 2008, **63**(12), 515–582.
4 S. Jenny, M. Masaya, T. Masato, Z. Jinlong, H. Yu, A. Masakazu and D. W. Bahnemann, *Chem. Rev.*, 2014, **114**(19), 9919–9986.
5 W. Changhua, S. Changlu, L. Yichun and L. Xinghua, *Inorg. Chem.*, 2009, **48**(3), 1105–1113.
6 L. Gonghu, N. M. Dimitrijevic, C. Le, J. M. Nichols, R. Tijana and K. A. Gray, *J. Am. Chem. Soc.*, 2008, **130**(16), 5402.
7 R. Zhang, D. Shen, X. Ming, F. Dan, L. Wei, G. Zheng, R. Che, A. A. Elzatahry and D. Zhao, *Adv. Energy Mater.*, 2014, **4**(8), 1289–1295.
8 A. Amtout and R. Leonelli, *Phys. Rev. B: Condens. Matter*, 1995, **51**(11), 6842–6851.
9 A. Fujishima and X. Zhang, *C. R. Chim.*, 2006, **9**(5), 750–760.
10 X. Lin, D. Fu, L. Hao and Z. Ding, *J. Environ. Sci.*, 2013, **25**(10), 2150–2156.
11 S. Larumbe, M. Monge and C. Gómez-Polo, *Appl. Surf. Sci.*, 2015, **327**, 490–497.
12 S. Sood, A. Umar, S. K. Mehta and S. K. Kansal, *J. Colloid Interface Sci.*, 2015, **450**, 213–223.
13 H. Feng, M. H. Zhang and L. E. Yu, *Appl. Catal., A*, 2012, **413–414**, 238–244.
14 N. Farhangi, R. R. Chowdhury, Y. Medina-Gonzalez, M. B. Ray and P. A. Charpentier, *Appl. Catal., B*, 2011, **110**, 25–32.

15 X. Yang, C. Cao, L. Erickson, K. Hohn, R. Maghirang and K. Klabunde, *Appl. Catal., B*, 2009, **91**(3), 657–662.
16 T. Morikawa, R. Asahi, T. Ohwaki, K. Aoki and Y. Taga, *Jpn. J. Appl. Phys.*, 2001, **40**(6A), L561–L563.
17 M. M. Rashad, E. M. Elsayed, M. S. Al-Kotb and A. E. Shalan, *J. Alloys Compd.*, 2013, **581**(5), 71–78.
18 C. Wang, Q. Q. Hu, J. Q. Huang, Z. H. Deng, H. L. Shi, L. Wu, Z. G. Liu and Y. G. Cao, *Int. J. Hydrogen Energy*, 2014, **39**(5), 1967–1971.
19 C. Wang, Q. Hu, J. Huang, L. Wu, Z. Deng, Z. Liu, Y. Liu and Y. Cao, *Appl. Surf. Sci.*, 2013, **283**, 188–192.
20 P. Gomathisankar, T. Noda, H. Katsumata, T. Suzuki and S. Kaneco, *Front. Chem. Sci. Eng.*, 2014, **8**(2), 197–202.
21 T. Sreethawong and S. Yoshikawa, *Catal. Commun.*, 2005, **6**(10), 661–668.
22 Q. Wang, A. Ning, B. Yan, H. Hang, J. Li, X. Lu, Y. Liu, F. Wang, Z. Li and Z. Lei, *Int. J. Hydrogen Energy*, 2013, **38**(25), 10739–10745.
23 A. V. Rosario and E. C. Pereira, *Appl. Catal., B*, 2014, **144**(2), 840–845.
24 X. Yue, S. Yi, R. Wang, Z. Zhang and S. Qiu, *J. Mater. Chem. A*, 2017, **5**(21), 10591–10598.
25 R. Marschall, *Adv. Funct. Mater.*, 2014, **24**(17), 2420.
26 Y. Jiaguo, L. Jingxiang, X. Wei, Z. Peng and J. Mietek, *J. Am. Chem. Soc.*, 2014, **136**(25), 8839–8842.
27 F. Mushtaq, A. Asani, M. Hoop, X. Z. Chen, D. Ahmed, B. J. Nelson and S. Pané, *Adv. Funct. Mater.*, 2016, **26**(38), 6995–7002.
28 C. Clavero, *Nat. Photonics*, 2014, **8**(2), 95–103.
29 M. Andreas, L. Michael, L. Karin, W. Gunnar and O. Lars, *J. Phys. Chem. B*, 2006, **110**(3), 1210–1220.
30 J. Yang, X. Zhang, C. Wang, P. Sun, L. Wang, B. Xia and Y. Liu, *Solid State Sci.*, 2012, **14**(1), 139–144.
31 Y. Kou, J. Yang, B. Li and S. Fu, *Mater. Res. Bull.*, 2015, **63**, 105–111.
32 W. Li, T. Bak, A. Atanacio and J. Nowotny, *Appl. Catal., B*, 2016, **198**, 243–253.
33 B. N. Joshi, H. Yoon, M. F. A. M. V. Hest and S. S. Yoon, *J. Am. Ceram. Soc.*, 2013, **96**(8), 2623–2627.
34 S. Khan, H. Cho, D. Kim, S. S. Han, K. H. Lee, S. H. Cho, T. Song and H. Choi, *Appl. Catal., B*, 2017, **206**, 520–530.
35 L. Kong, C. Wang, Z. Han, X. Zhang and Y. Liu, *J. Phys. Chem. C*, 2015, **119**(29), 16623–16632.
36 L. F. da Silva, W. Avansi, A. Catto, J. E. F. S. Rodrigues, M. Bernardi and V. Mastelaro, *Phys. Status Solidi A*, 2018, **215**(21), 1870049.
37 X. Yang, Y. Min, S. Li, D. Wang and P. Feng, *Catal. Sci. Technol.*, 2018, **8**(5), 1357–1365.
38 X. Yang, M. J. Zhang, Y. Min, M. Xu, Z. Mei, J. Liang, J. Hu, S. Yuan, S. Xiao and Y. Duan, *ACS Appl. Mater. Interfaces*, 2017, **9**(34), 29021.
39 J. Augustynski, *Electrochim. Acta*, 1993, **38**(1), 43–46.
40 T. V. D. Meulen, A. Mattson and L. Österlund, *J. Catal.*, 2007, **251**(1), 131–144.
41 Y. M. Xu, K. L. Lv, Z. G. Xiong, W. H. Leng, W. P. Du, D. Liu and X. J. Xue, *J. Phys. Chem. C*, 2007, **111**(111), 19024–19032.
42 H. Li, X. Shen, Y. Liu, L. Wang, J. Lei and J. Zhang, *J. Alloys Compd.*, 2015, **646**, 380–386.
43 X. Zhang, Y. Lin, D. He, J. Zhang, Z. Fan and T. Xie, *Chem. Phys. Lett.*, 2011, **504**(1), 71–75.
44 K. H. Hung, P. W. Lee, W. C. Hsu, H. C. Hsing, H. T. Chang and M. S. Wong, *J. Alloys Compd.*, 2011, **509**(42), 10190–10194.
45 F. Wang, G. Zhang, Z. Zhao, H. Tan, W. Yu, X. Zhang and Z. Sun, *RSC Adv.*, 2015, **5**(13), 9861–9864.
46 J. Y. Zheng, S. H. Bao, Y. Guo and K. Minoru, *Surf. Coat. Technol.*, 2014, **240**(7), 293–300.
47 T. L. Chen, Y. Hirose, T. Hitosugi and T. Hasegawa, *J. Phys. D: Appl. Phys.*, 2008, **41**(6), 3142–3147.
48 N. Yamada, T. Hitosugi, J. Kasai, N. L. H. Hoang, S. Nakao, Y. Hirose, T. Shimada and T. Hasegawa, *J. Appl. Phys.*, 2009, **105**(12), 252101-I05.
49 N. S. Kamarozaman, M. N. Asiah, Z. Aznilinda, R. A. Bakar, S. H. Herman and M. Rusop, *Appl. Mech. Mater.*, 2013, **393**, 63–67.
50 M. Landmann, E. Rauls and W. G. Schmidt, *J. Phys.: Condens. Matter*, 2012, **24**(19), 1614–1621.
51 J. Heyd, G. E. Scuseria and M. Ernzerhof, *J. Chem. Phys.*, 2003, **1181**(18), 8207–8215.
52 A. V. Krukau, O. A. Vydrov, A. F. Izmaylov and G. E. Scuseria, *J. Chem. Phys.*, 2006, **125**(22), 3865.
53 G. Kresse and J. Hafner, *Phys. Rev. B: Condens. Matter Mater. Phys.*, 1994, **49**(20), 14251.
54 Y. Hinuma, A. Grüneis, G. Kresse and F. Oba, *Phys. Rev. B: Condens. Matter Mater. Phys.*, 2014, **90**(15), 096401.
55 Y. Hinuma, F. Oba, K. Yu and I. Tanaka, *Phys. Rev. B: Condens. Matter Mater. Phys.*, 2012, **86**(24), 245433.
56 P. Deák, B. L. Aradi and T. Frauenheim, *J. Phys. Chem. C*, 2011, **115**(8), 3443–3446.
57 Z. Yong-Fan, L. Wei, L. Yi, D. Kai-Ning and L. Jun-Qian, *J. Phys. Chem. B*, 2005, **109**(41), 19270.
58 D. O. Scanlon, C. W. Dunnill, B. John, S. A. Shevlin, A. J. Logsdail, S. M. Woodley, C. R. A. Catlow, M. J. Powell, R. G. Palgrave and I. P. Parkin, *Nat. Mater.*, 2013, **12**(9), 798–801.
59 S. X. Zhang, D. C. Kundaliya, W. Yu, S. Dhar, S. Y. Young, L. G. Salamanca-Riba, S. B. Ogale, R. D. Vispute and T. Venkatesan, *J. Appl. Phys.*, 2007, **102**(1), 15.
60 Y. Furubayashi, N. Yamada, Y. Hirose, Y. Yamamoto, M. Otani, T. Hitosugi, T. Shimada and T. Hasegawa, *J. Appl. Phys.*, 2007, **101**(9), 093705.
61 L. E. Depero, L. Sangaletti, B. Allieri, E. Bontempi, R. Salari, M. Zocchi, C. Casale and M. Notaro, *J. Mater. Res.*, 1998, **13**(06), 1644–1649.
62 D. Chen, D. Yang, Q. Wang and Z. Jiang, *Ind. Eng. Chem. Res.*, 2006, **45**(12), 4110–4116.
63 N. Masahashi, Y. Mizukoshi, S. Semboshi and N. Ohtsu, *Appl. Catal., B*, 2009, **90**(1–2), 255–261.

